Defining a new process window for LPBF of Ti-6Al-4V based on micro-warping phenomena

Gianluca Buffa[a], Antonio Costa[b], Dina Palmeri[a], Gaetano Pollara[a] and Livan Fratini[a]

a Department of Engineering, University of Palermo, Palermo, Italy
b DICAR Department, University of Catania, Catania, Italy
*Corresponding author: gianluca.buffa@unipa.it

Abstract

Despite the many advantages that additive technologies have over subtractive ones, low porosity levels, good mechanical properties, and low residual stresses remain the most pressing issues that need further research. In particular, the latter can cause a mismatch between the desired geometry and the geometry that can be achieved. In this work, a process window for the Laser Powder Bed Fusion (LPBF) process of Ti-6Al-4V alloys, has been identified. The micro-warping phenomenon, which causes the deformation of the printed part during the printing job and the failure of the process, was taken into account together with the parts' strength, ductility, and porosity. The occurrence of micro-warping phenomena was assessed by the new Warping Alert (WA) parameter, which depends on the parameters P and v. It was found that, before balling, micro-warping limits the process window in the laser power (P) – laser velocity (v) plane. However, optimal mechanical performances can be found in the proximity of the micro-warping zone, thus making it extremely important to determine the WA threshold value to the process design.

Keywords: LPBF, micro-warping, Ti-6Al-4V, Porosity.

1. Introduction

Laser Powder Bed Fusion (LPBF), also known as selective laser melting (SLM) or direct metal laser melting (DMLM), uses a laser beam to melt metallic powders inside a specific area based on the cross-sectional slice of a three-dimensional CAD model.

Applications of the process involving the use of Ti-6Al-4V alloys are widespread in high-added-value sectors such as aerospace and biomedical [1]. Although additive technologies offer numerous advantages compared to subtractive technologies, a few critical points exist, the major ones being residual porosity levels, which can be critical for applications requiring high strength, low surface quality, and residual stresses, which can lead to warping phenomena [2]. These phenomena can, in turn, result in out-of-tolerance parts or even in the failure of the whole printing process, with detrimental effects on productivity and possible damage to some machine parts [3,4].

In the scientific literature, different studies can be found focusing on the determination of the relevant process window to be used to obtain high-density products [5,6]. Different levels of porosity are usually correlated with the energy input values [7,8]. When the energy is delivered to the powder bed continuously, the energy input, also known as laser fluence, can be considered as the following (eq. 1):

$$E_V = \frac{P}{h\,t\,v} \ (\text{J/mm}^3) \qquad (1)$$

If the hatch distance (h) and layer thickness (t) are kept constant is reasonable to use the line energy density (E_L) instead of the volumetric energy density (E_V). The E_L is expressed by the ratio between the laser power (P) and the scan speed (v) as shown in eq. 2 [9]:

$$E_L = \frac{P}{v} \ (\text{J/mm}) \qquad (2)$$

When a pulsed emission mode is adopted, instead, the interaction between the beam and the material depends on the distance between consecutive points (d_p) and the exposure time (t_{exp}) [10]. In this case, the laser fluence (F) is defined as (eq. 3):

$$F = \frac{P\,t_{exp}}{d_p\,h\,t} \ (\text{J/mm}^3) \qquad (3)$$

For given values of layer thickness and hatch spacing, and continuous laser emission mode, four process zones can be identified in the [P-v] plane, three of which highlighting high porosity zones, and one defining a high-density zone [11–14].

For very low scanning speed values, a zone of Over-Heating is found, denoting an excess of energy that prevents low defect samples from being obtained. Zones II, characterized by over-melting, and III, characterized by incomplete melting, demarcate the optimum density zone called zone I which is fully dense. In zone II, the process parameters result in excessive energy input, while in zone III they result in a reduced energy input that favors defect formation due to incomplete melting [13–16].

A few studies also explore the upper limit of zone I at optimum density, showing that for high values of both scanning speed and laser power, a further region of sample defect called balling effect is found. In particular, balling can occur at high laser powers and scanning speeds even with an optimal linear energy density, since the increase in laser power leads to an increase of the maximum temperature reached in the melt pool.

In turn, this induces a more intense Marangoni flow and, in the presence of Plateau-Rayleigh instability phenomena, produces the formation of balling-type defects [17–20]. The balling effect is caused by an instability of the melt pool, which fragments as it solidifies into separate spheres, thus causing the formation of discontinuous traces that inhibit the possibility of obtaining accurate geometries. Balling phenomena can also lead to high porosity levels along with delamination phenomena between layers due to non-uniform powder deposition on the layers [21,22].

Although useful knowledge can be derived from the above-cited research works, it is worth noting that the sole evaluation of density is not sufficient to determine the overall quality of a printed part, e.g. mechanical strength and ductility, as well as dimensional accuracy, should be also taken into account [23].

Moreover, a thorough examination of the process window in the proximity of the boundary that demarcates the high-density region from the area where micro-warping phenomena occur has not been documented in the existing literature. Previous studies by the authors have shown that in the zone delimiting the process parameter values that result in low porosity values, an upper threshold region can be identified, which marks the transition from an area of accurate geometry to an area in which surface micro-warping phenomena occur, especially near the edges of the produced parts, thus affecting the dimensional precision of the samples [24]. The set of all the experimental tests considered for the detection of the threshold value of the WA parameter explored a wide range of points, in the P,v plane, which fall in the Fully Dense zone. In particular, the limit LED values beyond which one falls either in the "Over melting" region or in the "Incomplete melting" region

have been taken into account. The lines of equation P=m*v define the fully dense zone when the LED parameter changes. For the micro-warping phenomenon, instead, as it can be observed in a previous paper by some of the authors [24], the P,v values are not fitted by a line but rather by a curve of type P*v= constant.

Plateau-Rayleigh instability is closely related to the balling phenomenon that occurs when the single trace, in the liquid state, is fragmented into distinct drops. In the present case, the phenomenon of Micro-Warping is a precursor of balling. It is manifested by process parameter values that do not determine Balling and for which the single track is continuous.

In the present work, an analysis of the effect of the process parameters P [W] and v [mm/s] on the dimensional accuracy of the products was carried out. The porosity and mechanical properties, in terms of Ultimate Tensile Strength (UTS) and Elongation To Failure (ETF), were also analyzed and related to the occurrence of micro-warping phenomena leading to the printing job failure or poor dimensional accuracy. By varying the Line Energy Density (LED = P/v J/mm), a threshold parameter identifying the occurrence of micro-warping, called Warping Alert (WA = Pv/1000 Jm/s^2), previously identified by the authors, was fine-tuned. Porosity, UTS, and ETF values were collected and related to occurring threshold conditions. Experimental investigations were conducted to characterize the top surface of Ti6Al4V alloy dog bone-shaped specimens produced by LPBF, in order to assess the influence of laser power and scanning speed on the geometric accuracy of the parts. In particular, for the samples that presented significant surface micro-warping phenomena, the printing process was interrupted and the extent of the dimensional deviation of the obtained geometry was measured.

2. Overview of the experiments

For the experiments, a gas-atomized spherical Ti6Al4V powder was used. The powder size shows a Gaussian distribution where d10 and d90 correspond to 20 μm and 63 μm, respectively. Samples were fabricated via LPBF on an SLM280HL (SLM Solutions, Lubeck, Germany) machine equipped with a continuous emission mode laser. Different combinations of laser power and scanning speed, maintaining constant values of hatch distance (120 μm), layer thickness (30 μm), scan strategy (0°), and build orientation (90°) has been used for the printing process. In detail, regarding the scan strategy, a value of 0° means that no rotation of the scanning vectors between

consecutive layers was adopted (Figure 1). Concerning the build orientation, 90° is the angle between the build platform and the part. The choice of build orientation equal to 90° was made to obtain specimens with a good compromise between mechanical strength and ductility [25]. The findings of a previous study by the authors, demonstrating the existence, in the P-v plane, of a transition zone between the sound parts and surface micro-warping ones, were used to determine proper ranges of the process parameters [24].

Table 1 Input process parameters for each considered process condition.

Id	P (W)	v (mm/s)	LED (J/mm)	WA (J m/s^2)
1	270	1,800	0.15	486
2	260	1,733	0.15	450
3	280	1,866	0.15	522
4	300	1,666	0.18	500
5	280	1,555	0.18	435
6	320	1,777	0.18	568
7	350	1,400	0.25	490
8	320	1,280	0.25	409
9	360	1,440	0.25	518
10	370	1,276	0.29	472
11	340	1,172	0.29	398
12	390	1,344	0.29	524
13	385	1,241	0.31	478
14	370	1,193	0.31	441
15	400	1,290	0.31	516

Specifically, five LED values were selected within zone I in the P-v plane, i.e. within the optimal density area of the process window.
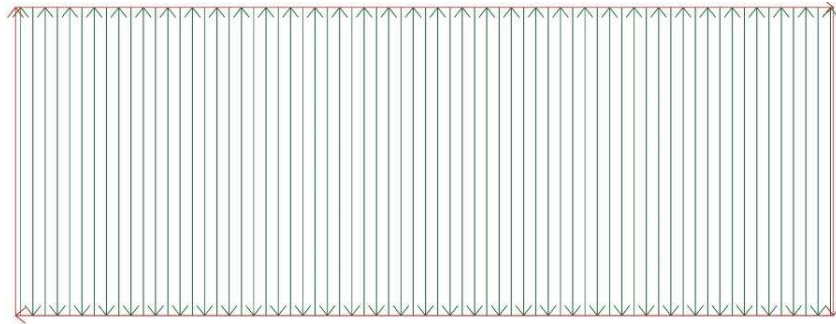
Fig. 1. Sketch of the scanning strategy adopted in this study for all the layers.

For each LED value, three different process conditions corresponding to three combinations of P and v were identified, thus resulting in 15 different case studies (Table 1). It is noted that the three experimental points were chosen so as to fall below, within and above the micro-warping transition zone above described. The warping alert parameter WA (Jm/s^2), as previously proposed by the authors [24], was calculated and it is shown in Table 1. Figure 2 shows the graphical representation of the considered case studies according to their LED values. It is observed that the points are located in the upper position of the "fully dense" zone, as it is known in the literature. This choice was driven by two reasons: (i) to investigate the possibility of increasing the range of parameter combinations resulting in sound joints; (ii) in a previous study by the authors [24], it was shown that in close proximity of the zone identified as the transition zone between sound and micro-warping parts, corresponding to high values of product between the power and the feed rate, progressive increases in the mechanical properties of the printed parts occurs under certain conditions. It is noted that the printing parameters recommended by the printer manufacturer (P=350 W and v=1400 mm/s) are included among the considered case studies. Finally, it is noted that the build orientation was chosen equal to 90° in order to minimize the surface area deposited per layer, thus making the printing process free of macro warping phenomena associated with the build-up of residual stresses when printing large surfaces.
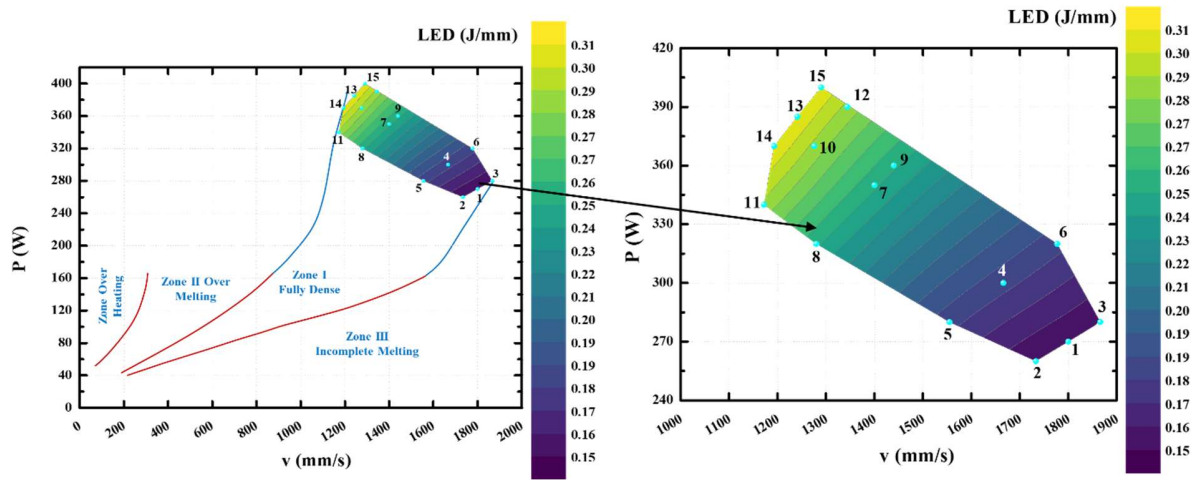
Fig. 2. Considered case studies obtained by extending (blue curves) literature process window (red curves) – experimental points in the P-v plane and contour color map of LED values.

The samples were printed with a dog-bone shape as a reduction of the ASTM/E8 and were tasted at a constant strain rate of 0.45 mm/min. The samples were characterized by a rectangular cross-section of 3 x 5 mm and a gauge length of 18 mm as illustrated in Figure 3.
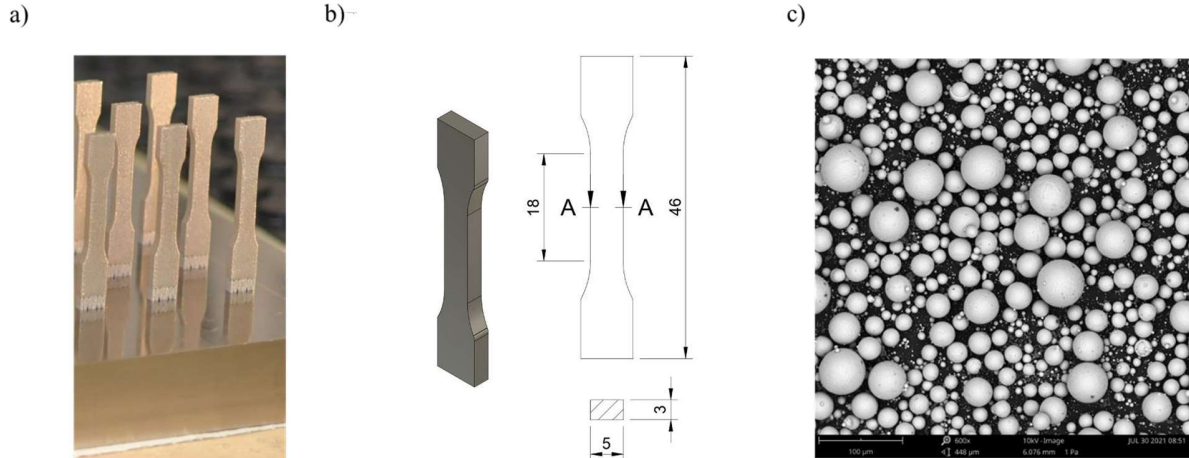

Fig. 3. (a) Printed specimens, (b), dog-bone sample dimensions, and (c) micrographic view of Ti-6Al-4V powder used in the experimental campaign.

In order to lessen the effects of the thermal gradient and prevent deformation, the titanium substrate on which the samples were printed was preheated to a temperature of 200° C. Argon was used to fill the printing chamber so that the oxygen concentration could be kept below 0.1%. Figure 3

depicts some of the printed samples, their geometry, and the micrograph of the Ti6Al4V powder utilized.

To determine the ultimate tensile strength (UTS) and the elongation to failure (ETF) of the parts, tests were conducted using a Galdabini Sun 5 universal testing machine with a maximum load capacity of 50 kN. The extension of the tensile samples during the tests was measured through extensometers. All the tests were repeated five times, and, in the following paragraphs, the average values are shown.

For samples exhibiting surface micro-warping phenomena, the dimensional deviation from the CAD geometry was quantitatively evaluated using the parameters A and B, as shown in Figure 4. The dimensional accuracy of the A and B measurements corresponds to ± 10 µm. The surfaces being analyzed were acquired with a magnification equal to 100X using a Stereo Microscope Olympus LS. In particular, parameter A indicates, in a lateral view of the printed samples, the maximal height, measured from the top surface of the specimen, of the protrusion resulting from the buildup of micro warping; on the other hand, parameter B measures the extension of the specimen area affected by micro-warping, starting from the edge of the sample.

For the measurement of the aforementioned parameters, calibrated macrographs of the lateral and top surfaces of the samples, taken when the printing process was stopped, were used.
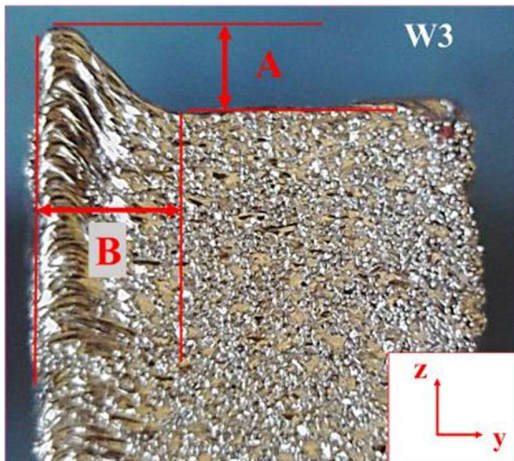

Fig. 4. Parameters A and B used for the surface warping phenomena quantification (specimen lateral view). The Z direction corresponds to the build direction.

Porosity was assessed by means of relative density (ρ_R) measurements using the Archimedes' method (ASTM B962-08), considering the density of water at 25°C of 0.9976 (g/cm^3) and the density of Ti-6Al-4V of 4.430 (g/cm^3) as reference values.

The method requires the utilization of an analytical balance in addition to a density kit. These two components, when combined, make it possible to determine the mass of the solid both while it is exposed to air and when it is submerged in a fluid, most commonly water. In this study, we utilized an analytical balance that had a resolution of 0.001 g as well as a container that housed the density kit.

The weight of the samples, both in water and in the air, was repeated five times, and the average value of the five measurements was used.

3. Results

3.1 Identification of the micro-warping threshold and micro-warping parameters

First of all, the threshold value of the WA parameter, identifying the boundary between the sound parts and the ones affected by micro-warping, was determined. To this scope, the transition zone identified in [24] was considered. In the case of samples produced with process parameters resulting in WA values beyond the warping transition zone (samples 3, 6, 9, 12,15), the printing process had to be stopped in order to before the sample was completed. In particular, the printed specimen exhibited micro-warping phenomena when the parameter WA exceeded the value of 500 (Jm/s^2).

Samples characterized by P and v resulting in a WA parameter value within the transition zone (samples 1, 4, 7, 10, 13) did not show homogeneous behavior during the printing process. In particular, sample 4 showed significant micro-warping phenomena that compromised the dimensional accuracy of the sample itself and required the early stop of the printing process.

Samples 1, 7, 10, and 13 maintained dimensional accuracy between the design geometry and the manufactured geometry. For samples that exhibited significant micro-warping phenomena, the printing procedure failed as a result of the accumulation of surface defects, which represented a hindrance to the recoater's movement for the deposition of the subsequent layers.

In turn, for samples characterized by WA values that remained below the warping transition zone (samples 2, 5, 8, 11, 14), the printing process could be completed without notable surface

dimensional deviations. The contour plots were designed by using the Thin Plate Spline (TPS) interpolation algorithm and by choosing the smoothing parameters that define the degree of smoothing. Considering that smaller numbers produce less smoothing the smoothing parameter was set equal to 0.001. The analysis of the results using contour color maps does not allow the specific variability of the experimental results to be displayed on each map. To make the maps independent of this specific variability of the experimental results, the average value of the five measurements was evaluated. The contour color maps were constructed considering the above-described average values.

Figure 5 shows the considered case studies in the P-v plane, with a contour map that highlights the value of the WA parameter within the same area as well as the transition zone (dashed black lines).
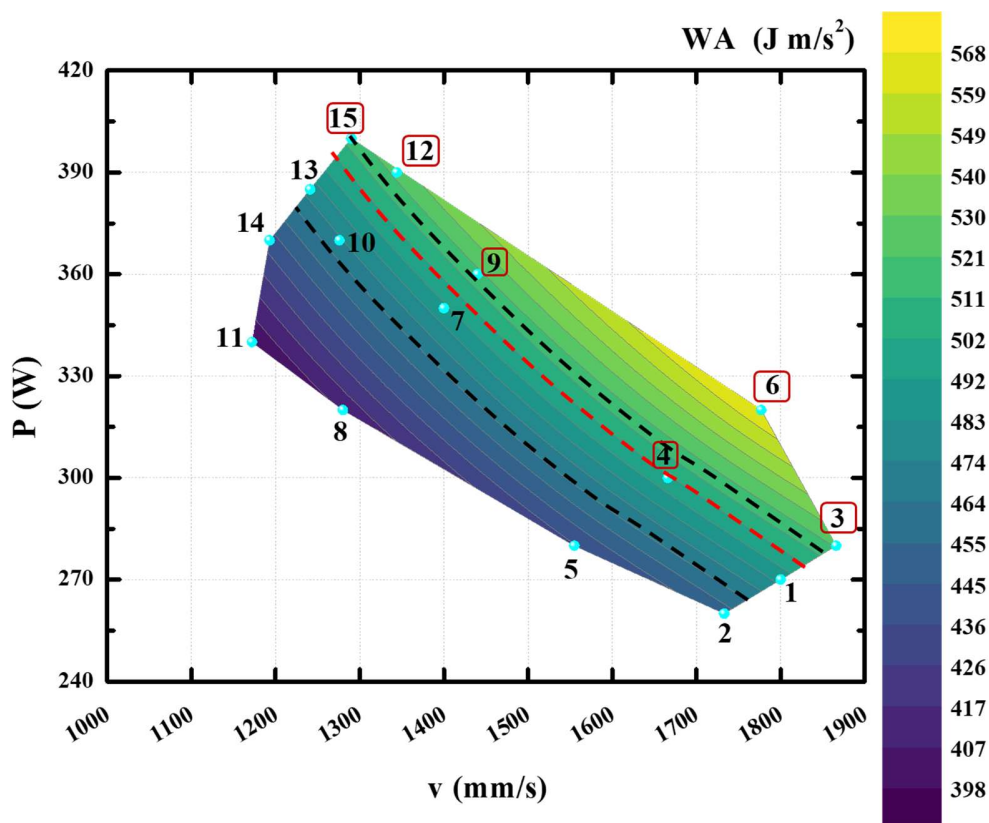

Fig. 5. WA parameter and micro-warped samples; the warping alert zone is indicated by black dashed lines, whereas the warping threshold is highlighted by a red line, in the red boxes the case studies which resulted in micro-warping.
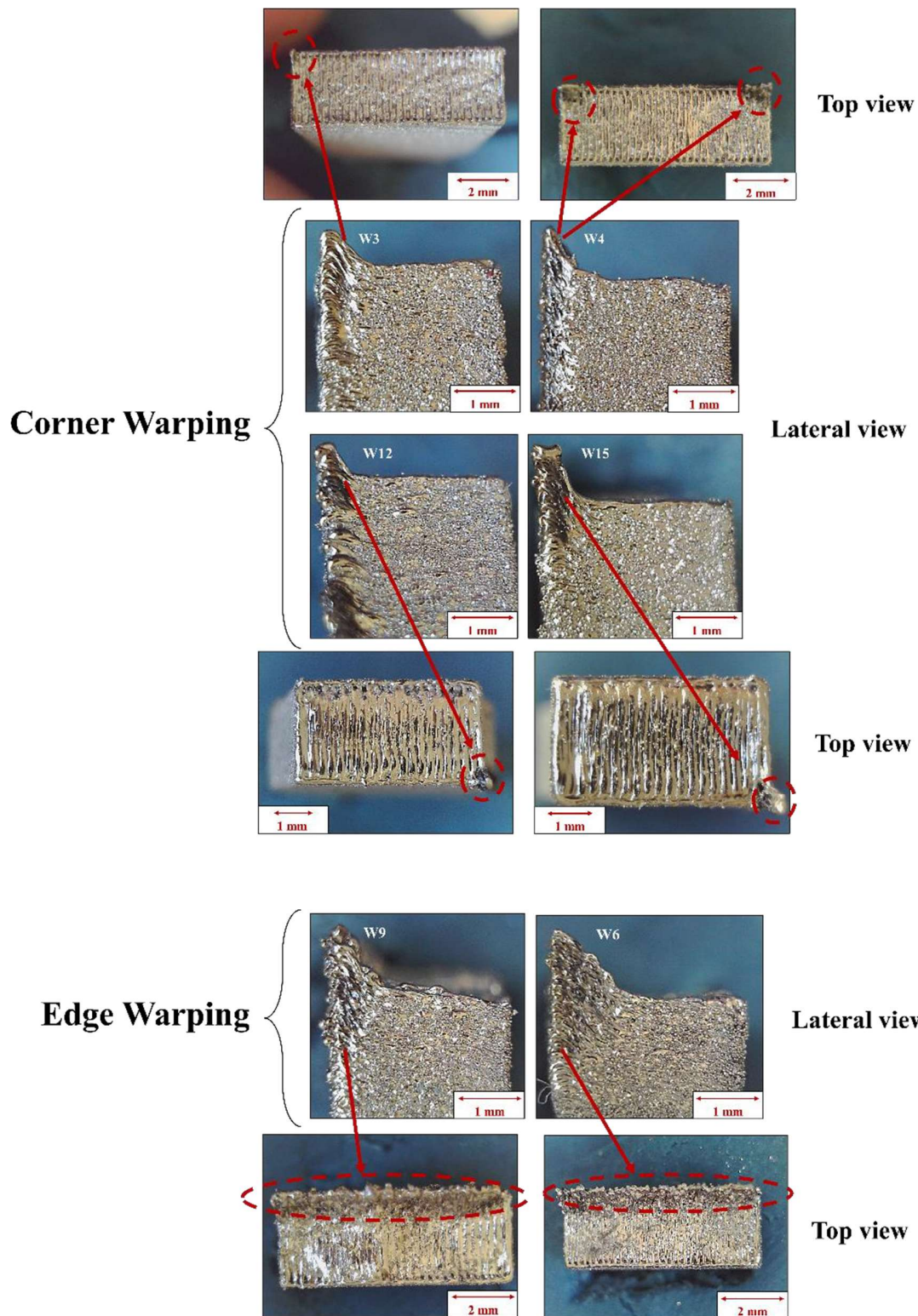
Fig. 6. Macrographs of samples characterized by surface micro-warping, top view and lateral view.

The case studies which resulted in micro-warping and, hence in the failure of the printing job, are marked with red boxes. These results enable the identification of the WA threshold value, equal to 500 Jm/s^2 (red line), for which the transition from the fully dense zone I to the micro-warping zone occurs. In this way, an upper boundary to the "fully dense" zone I can be identified based on the WA parameter. The micro-warping parameters, namely A and B, were measured in accordance with the previously described methodology. Figure 6 shows the macrographs of the top and lateral views of some of the samples printed with process parameters resulting in micro-warping phenomena, and hence in the failure and stop of the printing job. The top view macrograph was used to identify the specific type of micro-warping defect occurring. In particular, the study allowed the identification of two distinct defect morphologies. Samples 3, 4, 12, and 15 exhibit defects solely at the corners of the top surface of the sample (referred to as corner warping in the following)), whereas samples 9 and 6 display a more extensive micro-warping defect that affects not only the corners but also the entire edge of the top surface of the sample (referred to as edge warping in the following). The quantitative evaluation of A and B parameters, respectively, as measured in the conducted experiments, is shown in Figures 7 and 8.
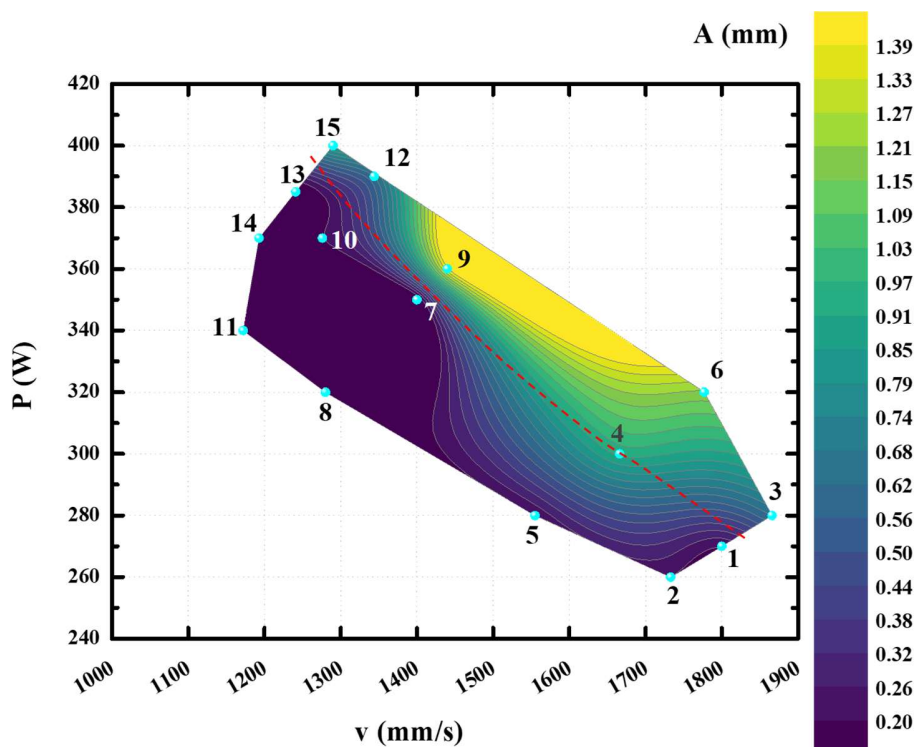
Fig. 7. Contour Plot for A micro-warping parameter. The dashed red line represents the warping threshold.

It was observed that the low values of both A and B can be found, for each of the LED values examined, when the WA parameter remains below the determined threshold value. However, with reference to the A parameter, a significant area, in the P-v plane, of very low value is observed for LED values exceeding 0.22 and for WA values below the warping threshold. A similar trend was observed for parameter B, although, in this case, a larger area characterized by extremely small values of parameter B can be observed. Parameters A and B exhibited the highest values for samples 6 and 9. The contour maps showing the trends of parameters A and B highlight that the phenomenon of micro-warping, which leads to significant geometric distortion of the sample not limited to the angular regions but extended over the entire edge, takes place when the magnitudes of P and v exceed specific levels.
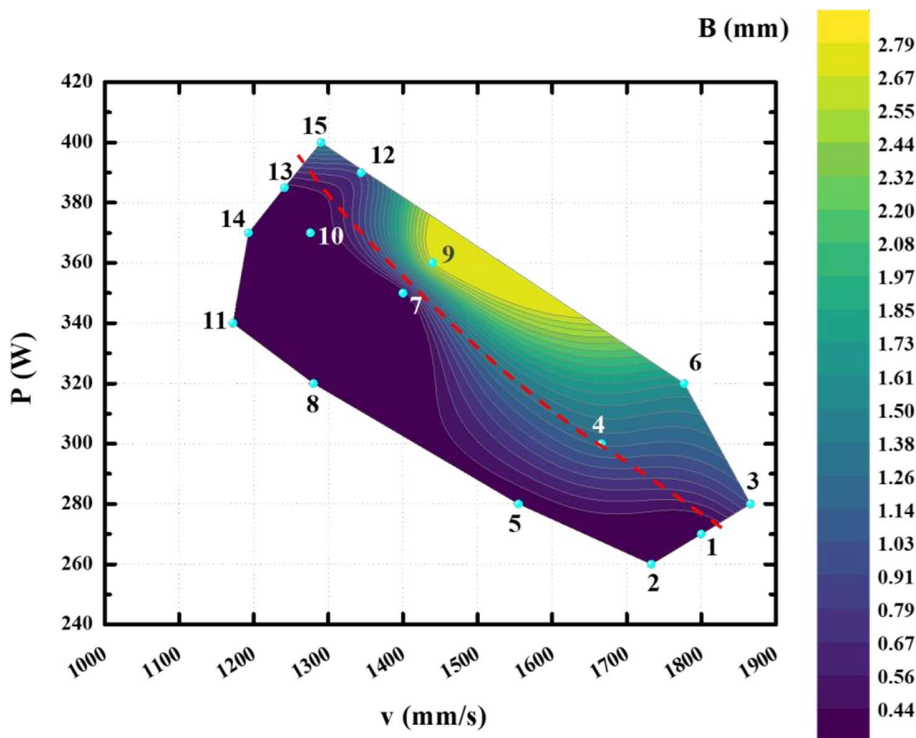

Fig. 8. Contour Plot for B micro-warping parameter. The dashed red line represents the warping threshold.

To justify the above phenomenon, it should be noted that for high values of P, the fluidity of the melt pool increases during the scanning of each line, whereas for high values of v, the kinetics of the material within the melt pool increases to the point where Marangoni-like flows occur, which favors the formation of track protrusions when the melt cools rapidly [19,20]. On the one hand, high P values combined with low v values result in strong melt fluidity and poor kinetics. These circumstances cause micro-warping phenomena only where the cooling rate of the material is high, i.e. at the corners. The same held for lower P and higher v values which result in lower fluidity and greater kinetics in the molten state. In the case of high values of both P and v, during the laser scanning process, there is a high fluidity of the melt in conjunction with high kinetics, which determines the formation of protrusions near the edges, which stabilize even at lower cooling rates than those occurring at the corners.

3.2 Tensile test results

The contour maps corresponding to the values of UTS and ETF are shown in Figures 9 and 10, respectively.
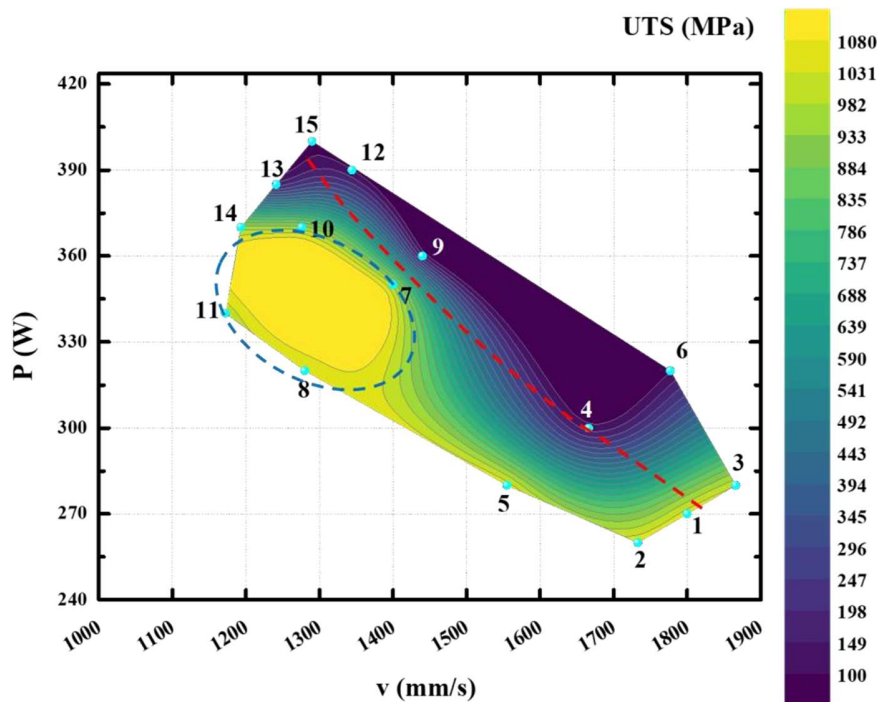

Fig. 9. Contour Plot for UTS results: dashed blue line delimits high UTS zone, dashed red line highlights the WA threshold.

The obtained results indicate that the material ultimate tensile strength (UTS) exceeds 1080 MPa for combinations of laser power and feed rate resulting in significantly different LED values, ranging from 0.24 J/mm to 0.31 J/mm. This high-strength region (dashed blue line in Figure 9) is below, yet quite close, to the WA threshold (dashed red line in Figure 9). Specifically, the WA parameters are found to be between 426 Jm/s^2 and 492 Jm/s^2. As far as the material ductility is regarded, a similar trend is found with respect to the one observed for UTS. The high ETF region corresponds to values of the WA parameter slightly lower than the ones previously highlighted. Specifically, the WA parameters are found to be between 407 Jm/s^2 and 492 Jm/s^2. The dashed blue curve in Figure 10 demarcates the best region for the ductility of the material near the transition threshold that separates zone I from the micro-warping zone.
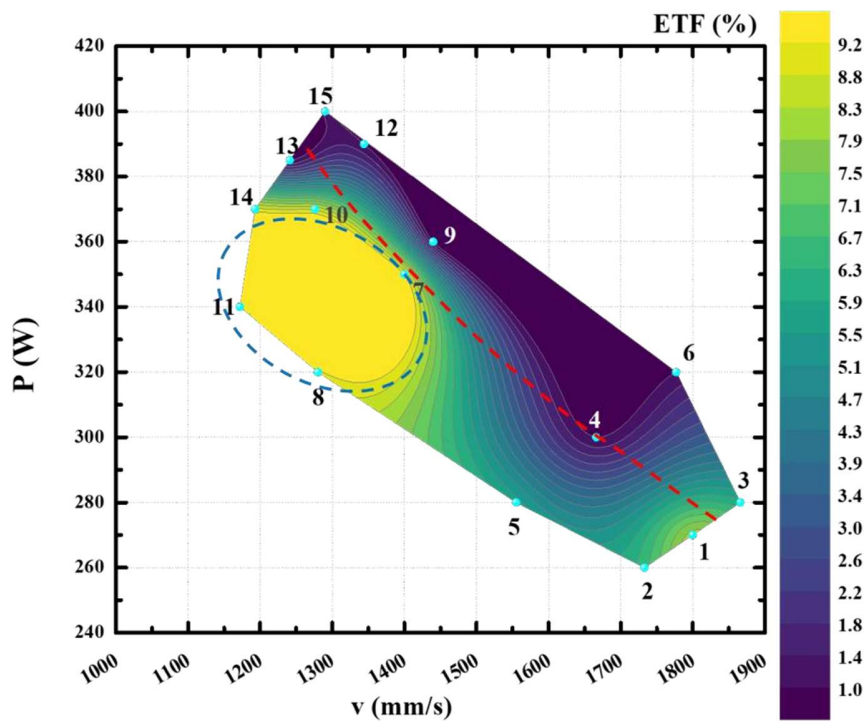

Fig. 10. Contour Plot for ETF results: dashed blue line delimits high UTS zone, dashed red line highlights the WA threshold.

3.3 Relative density results

Contour maps were also used to visualize high relative density areas in the P-v plane (Figure 11). The obtained results suggest that an increase in the parameter WA is associated with a decrease in

the relative density of the material. However, near the left and right boundaries of Zone I, the relative density tends to remain high even as the WA parameter increases and as long as the WA parameter stays below the threshold value.

Therefore, two regions representing the best relative density values can be identified, as illustrated in Figure 11 (dashed blue lines). These regions encompass a broad spectrum of LED values, ranging from 0.16 J/mm to 0.31 J/mm.

Based on the above observations as well as on previous literature [26], it can be stated that the area of greatest interest, in the P-v plane, considering both relative density and mechanical resistance, is identified by LED values ranging between 0.27 J/mm and 0.31 J/mm and WA values ranging between 407 Jm/s^2 and 492 Jm/s^2.
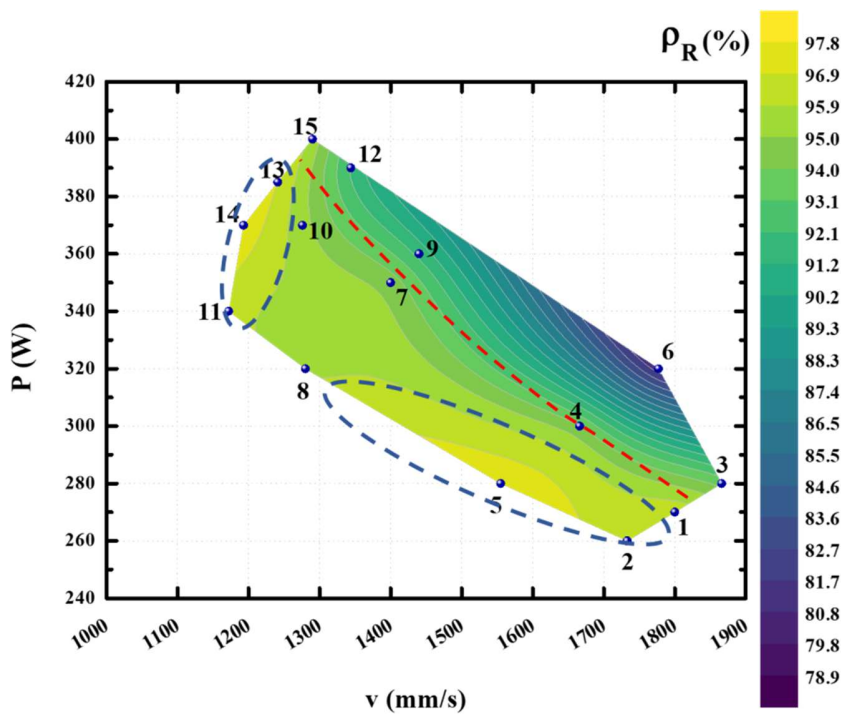

Fig. 11. Contour Plot for relative density results: dashed blue line delimits high UTS zones, dashed red line highlights the WA threshold.

It is worth noting that the highest UTS and ETF values were found inside the region bounded by specimens 7, 8, 11, 14, and 10 (Figures 9 and 10) and do not correspond to the region with the highest density. To explain this phenomenon, it should be noted that density measurements by Archimede's method give the average porosity of the sample but do not take into account its distribution within the sample itself. Previous studies [25,27] have shown that porosity tends to

increase along the building direction. This anisotropic porosity distribution can justify the trends obtained in terms of UTS andETFs. The correlation between the microstructure and the trends of the UTS, ETF, and density contour color maps has been clarified by conducting cross-sectional microstructural analyses. Samples W7 and W5 were selected for their different densities (with sample W7 having a lower one) and a similar UTS value, although sample W5 has a much lower ETF value than sample W7.As shown in Figure 12, three cross-sections were observed placed in the lower, middle, and upper parts of each sample. The microstructural analysis showed an inhomogeneous distribution of porosity along the building direction that justifies the fact that, for different density values, an analogous value of UTS is observed. In fact, as can be seen from the micrographs of the cross- sections of the W7 and W5 samples, the increase in porosity of the W7 sample occurs only in thelast print layers and therefore has no influence on the UTS value of the material. The values of ETF are more influenced by the value of LED, in fact, as indicated in Figure 10, the contour linesof the trend of the ETF parameter tend to be similar to the variability of the LED parameter in large areas of the P,v plane. In particular, with higher LED values (i.e. W7) an increased value ofETF is observed.
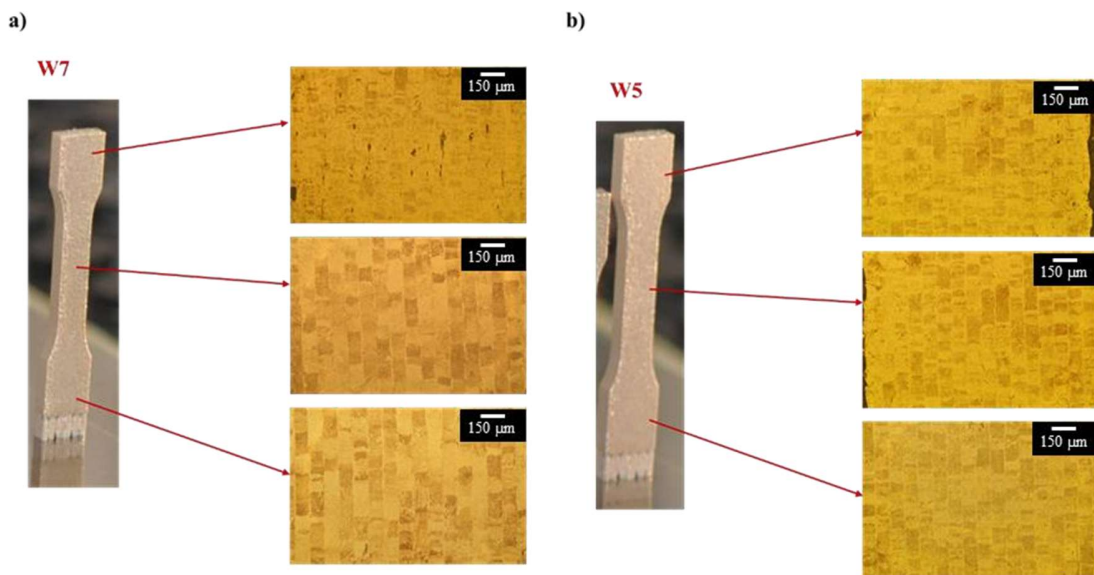

Fig. 12. Cross-sectional microstructural analysis on samples W7 a) and W5 b) placed in the lower, middle, and upper parts of samples.

4. New process window definition

The information acquired from analyzing the results shown in the previous paragraphs was used to modify and enhance the process window in the P-v plane, as currently known in the literature. As illustrated in Figure 13, the warping zone can be separated into three distinct areas. In two of them, which can be found along the borders of zones II and III, warping phenomena only involve the corners of the samples, and the geometric micro-warping parameters, A and B, have lower values. These areas have been defined as "corner warping" zones. In the third zone, defined as the "edge warping" zone, the warping phenomena are more significant and occur across a broad region of the sample.
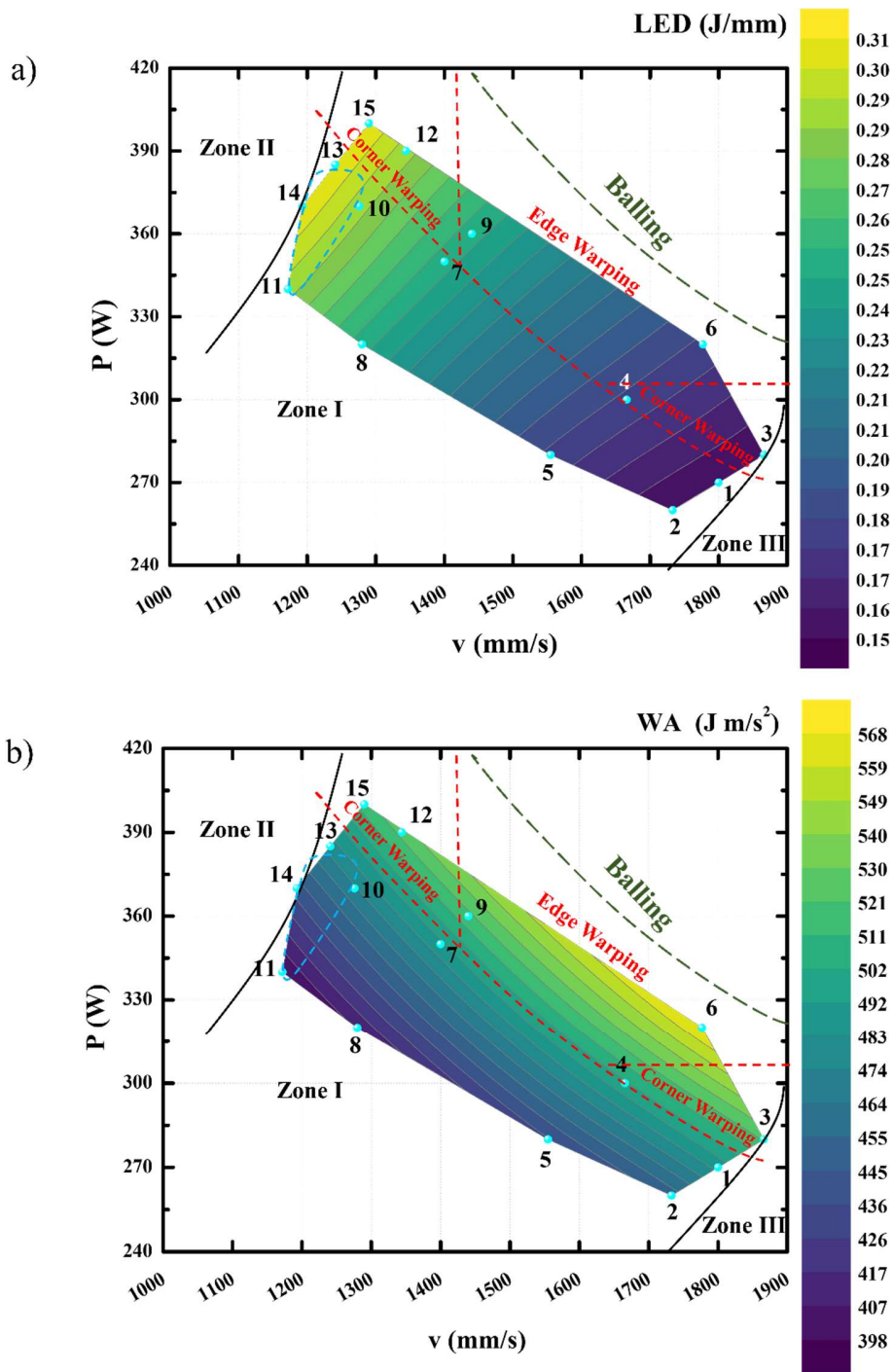
Fig. 13. Identification of transition zones and process windows in the P-v plane taking in consideration a) the WA parameter, and b) the LED values. The zone of process parameters that improve mechanical strength, ductility, and density is delimited by the dashed blue line the warping threshold is highlighted by a dashed red line.

Additionally, the combined analysis of the samples' mechanical properties and density enabled the identification of a particular region, within the domain of investigation, within which an ideal compromise between strength, ductility, and low porosity can be achieved (dashed blue line in Figure 13) for different combinations of LED and WA values. In detail, LED values between 0.27 J/mm and 0.31 J/mm and WA parameter values between 407 Jm/s^2 and 492 Jm/s^2, allowed to obtain, in addition to the best relative density values of the material, the best mechanical strength and ductility among the values considered in this study.

Finally, it is worth noting that the findings of the present research are related to the geometry under consideration, as well as the material (Ti-6Al-4V), printing method used (LPBF) and laser emission mode. Nevertheless, the definition of the process window can be extended to any geometry with similar thermal deposition conditions, according to the thermal parameters defined in [24,25], which allow the comparison of samples geometrically and dimensionally different from those characterized.

5. Summary and conclusions

In the paper, an experimental campaign for L-PBF of Ti-6Al-4V was carried out in order to expand and detail the process window, in the P-v plane, taking into account, besides mechanical and microstructural properties such as UTS, ETF, and density, the need to avoid micro-warping phenomena thus avoiding early failure of the printing job and preserving machine parts as the recoater and the wiper. The main findings of the present study are listed below:

- A new upper boundary for zone I ("fully dense") in the P-v plane was identified below the known limit corresponding to the balling defect. This upper bound corresponds to the occurrence of the micro-warping phenomenon;
- The phenomenon of micro-warping, which leads to early printing job failure and/or machine parts damage, takes place when the values of P and v exceed specific levels. In particular, the new Warping Alert parameter was used and a threshold value equal to 500 Jm/s^2 was identified;
- Depending on the combination of process parameters selected, micro-warping can be either limited to the corner regions of the printed sample top surface or extended over the entire edge. The corresponding areas have been highlighted in the P-v plane;

- A region of the P-v plane was identified, characterized by LED values between 0.27 J/mm and 0.31 J/mm and WA parameter values between 407 Jm/s^2 and 492 Jm/s^2, within which, in addition to having the best relative density values of the material, both the best mechanical strength and ductility values of the material are also guaranteed.

Finally, although the validity of the presented results is limited to the L-PBF of Ti-6Al-4V, the adopted methodology, as part of the possibility of future investigations and work, may be used for other materials and/or AM processes to investigate the presence of a possible WA threshold to predict micro-warping and establish more accurate process windows.

References

[1] Tepylo, N., Huang, X., Patnaik, P. C., 1 Nov 2019, Laser-Based Additive Manufacturing Technologies for Aerospace Applications, *Advanced Engineering Materials*. Wiley-VCH Verlag.

[2] Kasperovich, G., Haubrich, J., Gussone, J., Requena, G., 2016, Correlation between porosity and processing parameters in TiAl6V4 produced by selective laser melting, Materials and Design, 105:160–170, DOI:10.1016/j.matdes.2016.05.070.

[3] Wang, D., Dou, W., Yang, Y., 2018, Research on selective laser melting of Ti6Al4V: Surface morphologies, optimized processing zone, and ductility improvement mechanism, Metals, 8/7, DOI:10.3390/met8070471.

[4] DI Cataldo, S., Vinco, S., Urgese, G., Calignano, F., Ficarra, E., et al., 1 Apr 2021, Optimizing Quality Inspection and Control in Powder Bed Metal Additive Manufacturing: Challenges and Research Directions, *Proceedings of the IEEE*. Institute of Electrical and Electronics Engineers Inc., pp. 326–346.

[5] Xuan, C., 2023, A study of microstructural factors governing strength and ductility of titanium alloys fabricated by powder bed fusion additive manufacturing, Journal of Alloys and Compounds, 952, DOI:10.1016/j.jallcom.2023.170094.

[6] Lim, S., Murugan, S. P., Park, J., Lee, H., Jo, I., et al., 2023, Process window prediction in stainless steel selective laser melting using various energy densities: laser power, scan speed, and defocusing distance, Materials Research Express, 10/7, DOI:10.1088/2053-1591/ace67d.

[7] Gunenthiram, V., Peyre, P., Schneider, M., Dal, M., Coste, F., et al., 2017, Analysis of laser–melt pool–powder bed interaction during the selective laser melting of a stainless steel, Journal of Laser Applications, 29/2, DOI:10.2351/1.4983259.

[8] Liu, W., Chen, C., Shuai, S., Zhao, R., Liu, L., et al., 2020, Study of pore defect and mechanical properties in selective laser melted Ti6Al4V alloy based on X-ray computed tomography, Materials Science and Engineering: A, 797, DOI:10.1016/j.msea.2020.139981.

[9]   Cacace, S., Semeraro, Q., 2018, About Fluence and Process Parameters on Maraging Steel Processed by Selective Laser Melting: Do They Convey the Same Information?, International Journal of Precision Engineering and Manufacturing, 19/12:1873–1884, DOI:10.1007/s12541-018-0204-y.

[10]   Biffi, C. A., Fiocchi, J., Valenza, F., Bassani, P., Tuissi, A., 2020, Selective Laser Melting of NiTi Shape Memory Alloy: Processability, Microstructure, and Superelasticity, Shape Memory and Superelasticity, 6/3:342–353, DOI:10.1007/s40830-020-00298-8.

[11]   Oliveira, J. P., LaLonde, A. D., Ma, J., 2020, Processing parameters in laser powder bed fusion metal additive manufacturing, Materials and Design, 193, DOI:10.1016/j.matdes.2020.108762.

[12]   Cao, S., Zou, Y., Lim, C. V. S., Wu, X., 2021, Review of laser powder bed fusion (LPBF) fabricated Ti-6Al-4V: process, post-process treatment, microstructure, and property, Light: Advanced Manufacturing, 2/3, DOI:10.37188/lam.2021.020.

[13]   Gorsse, S., Hutchinson, C., Gouné, M., Banerjee, R., 31 Dec 2017, Additive manufacturing of metals: a brief review of the characteristic microstructures and properties of steels, Ti-6Al-4V and high-entropy alloys, *Science and Technology of Advanced Materials*. Taylor and Francis Ltd., pp. 584–610.

[14]   Gong, H., Rafi, K., Gu, H., Starr, T., Stucker, B., 2014, Analysis of defect generation in Ti-6Al-4V parts made using powder bed fusion additive manufacturing processes, Additive Manufacturing, 1:87–98, DOI:10.1016/j.addma.2014.08.002.

[15]   Zhang, B., Li, Y., Bai, Q., 1 May 2017, Defect Formation Mechanisms in Selective Laser Melting: A Review, *Chinese Journal of Mechanical Engineering (English Edition)*. Chinese Mechanical Engineering Society, pp. 515–527.

[16]   Majumdar, T., Bazin, T., Ribeiro, E. M. C., Frith, J. E., Birbilis, N., 2019, Understanding the effects of PBF process parameter interplay on Ti-6Al-4V surface properties, PLoS ONE, 14/8, DOI:10.1371/journal.pone.0221198.

[17]   Gunenthiram, V., Peyre, P., Schneider, M., Dal, M., Coste, F., et al., 2018, Experimental analysis of spatter generation and melt-pool behavior during the powder bed laser beam melting process, Journal of Materials Processing Technology, 251:376–386, DOI:10.1016/j.jmatprotec.2017.08.012.

[18]   Qiu, C., Panwisawas, C., Ward, M., Basoalto, H. C., Brooks, J. W., et al., 2015, On the role of melt flow into the surface structure and porosity development during selective laser melting, Acta Materialia, 96:72–79, DOI:10.1016/j.actamat.2015.06.004.

[19]   Yuan, W., Chen, H., Cheng, T., Wei, Q., 2020, Effects of laser scanning speeds on different states of the molten pool during selective laser melting: Simulation and experiment, Materials and Design, 189, DOI:10.1016/j.matdes.2020.108542.

[20]   Zhang, T., Li, H., Liu, S., Shen, S., Xie, H., et al., 2019, Evolution of molten pool during selective laser melting of Ti-6Al-4V, Journal of Physics D: Applied Physics, 52/5, DOI:10.1088/1361-6463/aaee04.

[21] Yasa, E., Deckers, J., Kruth, J. P., 2011, The investigation of the influence of laser re-melting on density, surface quality and microstructure of selective laser melting parts, Rapid Prototyping Journal, 17/5:312–327, DOI:10.1108/13552541111156450.

[22] Scipioni Bertoli, U., Wolfer, A. J., Matthews, M. J., Delplanque, J. P. R., Schoenung, J. M., 2017, On the limitations of Volumetric Energy Density as a design parameter for Selective Laser Melting, Materials and Design, 113:331–340, DOI:10.1016/j.matdes.2016.10.037.

[23] Javidrad, H. R., Ghanbari, M., Javidrad, F., 2021, Effect of scanning pattern and volumetric energy density on the properties of selective laser melting Ti-6Al-4V specimens, Journal of Materials Research and Technology, 12:989–998, DOI:10.1016/j.jmrt.2021.03.044.

[24] Buffa, G., Costa, A., Palmeri, D., Pollara, G., Barcellona, A., et al., 2023, A new control parameter to predict micro-warping-induced job failure in LPBF of TI6AL4V titanium alloy, International Journal of Advanced Manufacturing Technology, 126/3–4, DOI:10.1007/s00170-023-11179-6.

[25] Palmeri, D., Buffa, G., Pollara, G., Fratini, L., 2022, Sample building orientation effect on porosity and mechanical properties in Selective Laser Melting of Ti6Al4V titanium alloy, Materials Science and Engineering: A, 830/November 2021:142306, DOI:10.1016/j.msea.2021.142306.

[26] Zhao, R., Chen, C., Wang, W., Cao, T., Shuai, S., et al., 2022, On the role of volumetric energy density in the microstructure and mechanical properties of laser powder bed fusion Ti-6Al-4V alloy, Additive Manufacturing, 51:102605, DOI:10.1016/j.addma.2022.102605.

[27] Palmeri, D., Buffa, G., Pollara, G., Fratini, L., 2021, The Effect of Building Direction on Microstructure and Microhardness during Selective Laser Melting of Ti6Al4V Titanium Alloy, Journal of Materials Engineering and Performance, /Ref 12, DOI:10.1007/s11665-021-06039-x.

Appendix A

Experimental data measured for the considered case studies

Id	P (W)	v (mm/s)	LED (J/mm)	WA (J m/s^2)	ETF (%)	UTS (MPa)	A (mm)	B (mm)	ρ_R (%)
1	270	1800	0.15	486	8.11±0.08	1074±25	0.21±0.01	0.21±0.02	97.6±0.5
2	260	1733	0.15	450	6.60±0.10	1066±14	0.22±0.03	0.16±0.05	95.0±0.2
3	280	1866	0.15	522	6.08±0.09	1030±15	0.62±0.08	0.91±0.07	94.5±0.1
4	300	1666	0.18	500	<1	<100	0.93±0.09	1.17±0.09	96.0±0.2
5	280	1555	0.18	435	5.65±0.05	1077±21	0.21±0.02	0.3±0.01	97.1±0.6
6	320	1777	0.18	568	<1	<100	1.2±0.09	1.63±0.10	78.9±0.7
7	350	1400	0.25	490	9.16±0.07	1033±12	0.15±0.03	0.31±0.08	95.7±0.5
8	320	1280	0.25	409	9.09±0.04	1023±9	0.22±0.01	0.42±0.02	95.4±0.9
9	360	1440	0.25	518	<1	<100	1.39±0.08	2.79±0.09	91.8±0.7
10	370	1276	0.29	472	8.65±0.10	992±12	0.21±0.02	0.32±0.03	95.1±0.1
11	340	1172	0.29	398	9.11±0.05	980±15	0.16±0.01	0.41±0.05	95.8±0.6
12	390	1344	0.29	524	<1	<100	0.61±0.09	0.85±0.07	90.2±0.8

13	385	1241	0.31	478	<1	<100	0.13±0.02	0.43±0.02	97.0±0.5
14	370	1193	0.31	441	8.79±0.07	981±18	0.23±0.01	0.32±0.01	97.8±0.4
15	400	1290	0.31	516	<1	<100	0.89±0.09	1.46±0.08	97.1±0.8